On Reynolds Number Dependence of Micro-ramp-Induced Transition

Ye, Qingqing; Schrijer, Ferdinand; Scarano, Fulvio

Publication date
2016

Document Version
Final published version

Published in
Proceedings of the 18th International Symposium on the Application of Laser and Imaging Techniques to Fluid Mechanics

Citation (APA)
Ye, Q., Schrijer, F., & Scarano, F. (2016). On Reynolds Number Dependence of Micro-ramp-Induced Transition. In *Proceedings of the 18th International Symposium on the Application of Laser and Imaging Techniques to Fluid Mechanics* Springer.

18TH LISBON 2016
INTERNATIONAL SYMPOSIUM
ON APPLICATIONS OF LASER AND IMAGING TECHNIQUES TO FLUID MECHANICS
FROM 4 TO 7 OF JULY

PROCEEDINGS
OF THE
18th INTERNATIONAL SYMPOSIUM ON APPLICATION OF LASER AND IMAGING TECHNIQUES TO FLUID MECHANICS

On Reynolds Number Dependence of Micro-ramp-Induced Transition

Qingqing Ye[1,*], Ferry F. J. Schrijer[1], Fulvio Scarano[1]
1: Faculty of Aerospace Engineering, Delft University of Technology, The Netherlands
* Correspondent author: q.ye-1@tudelft.nl

Keywords: Boundary layer transition, stability, micro-ramp, Reynolds number, tomographic PIV, POD

ABSTRACT

The transitional flow features past a micro-ramp are investigated in the incompressible flow regime at critical and supercritical roughness-height based Reynolds number (Re_h). Tomographic PIV is adopted as the diagnostic technique to identify the instantaneous three-dimensional flow behaviour in the domain of 73 ramp height streamwise. The instantaneous and time-averaged flow topology are characterized in detail focusing on the influence of Reynolds number. A main difference is the longer streamwise presence range of primary vortex pair in the time-averaged flow topology at critical Re_h compared with supercritical condition, resulting in different type modification to the mean flow. The transition process is significantly delayed when decreasing Re_h. By performing Proper Orthogonal Decomposition (POD) analysis, two major types of eigenmodes with symmetric and asymmetric spatial distribution of velocity fluctuations in the near wake are observed, corresponding to the presence vortex shedding and sinuous wiggling motion respectively. The correlation between the former POD modes and the transition process strongly depends on Re_h.

1. Introduction

The role of surface roughness on boundary layer transition is of significant importance due to its impact in aerodynamic and aero-thermodynamic problems. Typically, the effect of roughness elements in promoting boundary layer transition is estimated by the roughness-height based Reynolds number, defined as $Re_h=u_h \times h/\nu$, where h is the roughness height and u_h is the streamwise velocity at that height (Tani 1969, van Driest and McCauley 1960). For a two dimensional roughness element without spanwise variation (e.g. step, gap or ribbon), the natural transition process is promoted by amplification of Tollmien-Schlichting (TS) waves at the downstream separation region of the roughness (Klebanoff and Tidstrom 1972). Increasing Re_h the transition location gradually moves upstream, closer to the roughness element. For three dimensional distributed or isolated roughness, a critical value of Re_h was obtained by experiments (Tani et al. 1962). When exceeding this value, transition will rapidly move upstream. Instead, below the critical Re_h, the flow in the wake of the roughness element remains stable. Klebanoff et al. (1992) proposed an empirical estimate of the critical Re_h for three-dimensional isolated roughness with aspect ratio (h/c) of unity. Based on existing experimental results, they proposed that $Re_{h,crit}$ lies in the range between 600 and 900 for incompressible flows. The empirical correlation offers a basic guideline for prediction of forced transition. However, the critical Reynolds number is still influenced by many factors, such as roughness shape and freestream disturbance level, questioning the generality of the proposed value. Moreover, the physical mechanism of roughness induced transition behind three-dimensional roughness elements at different Reynolds numbers is far from being fully understood and needs to be further consolidated. In order to inquire the fidelity of numerical simulations to predict transition, a more accurate and detailed experimental characterization of the flow behaviour is necessary.

In a laminar boundary layer, a three-dimensional isolated roughness element introduces a spanwise deflection of the velocity field. A circulatory motion is induced in both upstream and downstream separation region, leading to the formation of streamwise vortices in the wake (Fransson et al. 2004). The streamwise vortices induce an upwash motion on one side, transporting low momentum fluid away from the wall, and on the other side, they sweep high-momentum fluid towards the wall, resulting in the formation of low- and high-speed streaks which modulate the surface shear in the spanwise direction. Similarly, in the bypass transition process, the formation of velocity streaks through the 'lift-up' mechanism takes over the role of T-S waves in the process of the growth of the perturbations (Landahl 1990). Once the streak amplitude exceeds a critical value, the streak will be subject to a secondary instability, with either sinuous or varicose modulation, and finally breaks down into turbulence (Andersson et al. 2001).

The transition process shows strong dependence on Re_h, which affects the streak amplitude, length scales and perturbation growth rate. Ergin and White (2006) studied the transitional flow over a spanwise array of cylinder-shape roughness by using hotwire anemometry at various Re_h, ranging from subcritical to supercritical conditions. The presence of high velocity fluctuations located at the inflection point of the velocity profile indicates a possible effect of Kelvin-Helmholtz instability on transition. They also found that the growth rate of the disturbances increases rapidly with the increase of Re_h. As a result, at supercritical conditions, the disturbances spread laterally along the wake span and lead to transition to turbulence. On the other hand, in the subcritical condition, the disturbances are stabilized before transition can occur. In the recent direct numerical simulation conducted by Loiseau et al. (2014), velocity streaks are observed in the wake. Increasing Re_h leads to a longer streamwise persistence of a low speed region close to the spanwise symmetry plane. The increased amplitude of streaks makes the wake flow more prone to local streak instability.

Despite the intensive research on the effect of Reynolds number on roughness induced transition, most attention has been paid to the statistical analysis of perturbation growth and modal analysis in incompressible flow. Detailed analysis of the instantaneous flow organization depending upon the Reynolds number is necessary. Ye et al. (2016a, 2016b) measured the three-dimensional vortical structures in the wake of isolated roughness elements having different geometries (cylinder, square, hemisphere and micro-ramp) at supercritical Re_h using tomographic PIV. The flow pattern is well captured with a system of multiple counter-rotating vortex pairs in the near wake region. The instantaneous flow organization reveals the onset of hairpin vortices, following different evolution processes towards transition in the wake of various elements. As the former study only dealt with the supercritical condition, the unsteady flow behaviour closer to critical Re_h needs to be explored. Furthermore, it is particularly desired to identify the vortical structures that may contribute to the instability mechanism, leading to the interest in Proper Orthogonal Decomposition (POD), which is an efficient tool for data reduction in the field of fluid mechanics (Sirovich 1987). The obtained eigenmode can shed light on the dominant flow features and facilitate the reduced order description of the flow field.

The present investigation employs tomographic PIV to capture the three-dimensional aspects of the evolution process towards transition in the wake behind a micro-ramp. The experiments are conducted covering both critical and supercritical Re_h flow conditions. The system of streamwise vortices as well as the induced velocity distribution is identified in the time-averaged flow topology. The influence of Re_h on the instantaneous flow organization is visualized by the iso-surface of λ_2 criterion. The full article corroborates the analysis with a statistical characterization of the velocity fluctuations. The POD analysis returns the most energetic spatial modes, which are associated to the symmetric and asymmetric components of the growing velocity fluctuations.

2. Experiment setup and data reduction

2.1 Wind tunnel, flow conditions and micro-ramp geometry

The experiments are conducted in the open jet low-speed wind tunnel at the Aerodynamic Laboratories of Delft University of Technology. The wind tunnel has an exit of 0.4×0.4m^2

following a contraction ratio of 9:1. An aluminum flat plate with a length of 700mm, width of 400mm and a thickness of 10mm is placed at the mid-plane of the test section. The micro-ramp with 2mm height (h) and 4mm span (c) is placed along the centreline at 290mm downstream of the plate leading edge. The length (l) of micro-ramp is 4.5mm, resulting in an incidence angle (β) and half sweep angle (α) of 24°, as shown in Fig. 1. The x, y, z axes of the coordinate system is defined with respect to the streamwise, wall-normal and spanwise direction. The origin of the coordinate axis (o) is located on the symmetry plane at the wall, halfway the micro-ramp chord.

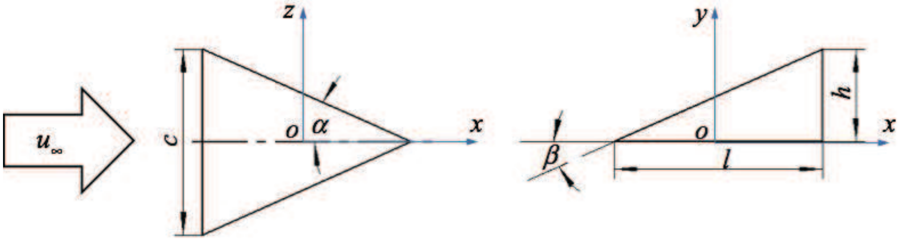

Fig. 1. Micro-ramp geometry and coordinate definition, top and side view.

The experiments are carried out at a freestream velocity u_∞ = 5 and 10m/s. The corresponding ramp height based Reynolds number Re_h is 465 and 1170, respectively. Based on the roughness aspect ratio h/c of 0.5, the critical Re_h ranges from 455 to 682, indicating critical and supercritical conditions for the current experiments (Klebanoff et al. 1955, Von Doenhoff and Braslow 1961). The undisturbed laminar boundary layer thickness (δ_{99}) (without the roughness element) is measured to be 4.74 and 3.26mm respectively. The resulting ratio between roughness height and boundary layer thickness is h/δ = 0.42 and 0.61. The shape factor of the undisturbed boundary layer is 2.59, indicating a laminar regime of the flow.

2.2 Tomographic PIV

The tomographic PIV system features four LaVision *Imager Pro LX* interline CCD cameras (4872×3248pixels, 7.4μm/pixel) arranged along an arc with a maximum aperture angle of β = 60° as shown in Fig. 2. The cameras are equipped with objectives of 105mm focal length and tilted to comply with the Scheimpflug condition. The aperture was set at $f_\#$=11, resulting in a focal depth of 8.4mm. The flow was seeded with a SAFEX fog machine that generates water-glycol droplets of approximately 1μm diameter. The seeding concentration is carefully adjusted at approximately 4particles/mm^3. The measurement region was illuminated with a Quantel *CFR PIV-200* Nd:YAG laser (200mJ/pulse, 532nm wavelength, 9ns pulse duration). The pulse separation time was set to 60 and 30μs, yielding a particle displacement of 10pixels in the free stream. The region of interest of the camera was cropped in the vertical direction resulting in an active sensor size of 4872 × 1500pixels. The corresponding measurement volume size is 145(x) × 6(y) × 45(z)mm^3 (72.5h × 3h × 22.5h), resulting in a digital image resolution of 33.6pixel/mm. The measurement domain begins 5mm behind the roughness centre and it covers approximately 70 heights. In the wall normal direction, the domain covers three ramp heights. Each dataset consists of 200 snapshots acquired at a frequency of 1.5Hz.

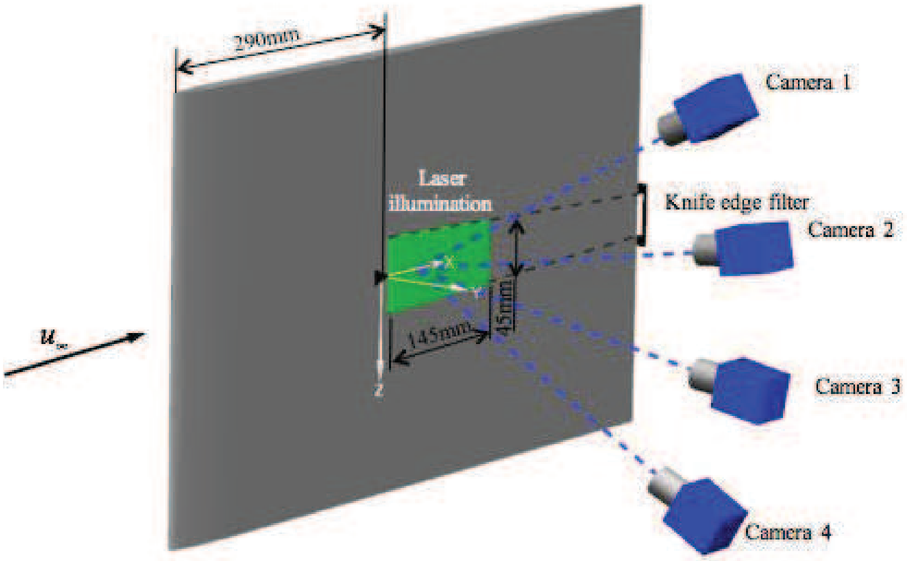

Fig. 2. Layout of experiment with schematic of illumination and imaging system.

LaVision *Davis 8* is used for system synchronization, calibration, data acquisition and processing. A custom-made calibration target is used for the calibration that establishes the relation between object and image space. Further corrections reducing misalignment errors to below 0.1 pixels are obtained using the 3D self-calibration technique (Wieneke 2008). The raw images are pre-processed by the subtraction of pixel time-minimum and of the spatial minimum from a kernel of 31×31 pixels. Image intensity was homogenized by normalization against the local average (kernel of 51×51 pixels). The measurement volume is reconstructed using the CSMART algorithm (Atkinson and Soria 2009). Spatial cross-correlation analysis is performed with a custom software (FLUERE, Lynch (2015)) performing multi-grid and volume deformation interrogation using a final interrogation volume of 40×20×40voxels (1.13×0.56×1.13mm^3), with an overlap of 75% between neighbouring interrogation windows. The resulting spatial resolution enables the detection of vortex structure down to half a roughness height. Outliers are detected using the normalized median filter proposed by Westerweel and Scarano (2005) and replaced with interpolated neighbouring values.

2.3 Proper Orthogonal Decomposition

Proper orthogonal decomposition (POD) is a well-established procedure introduced into fluid mechanics to statistically identify dominant coherent structures in complex flows (Lumley 1967). The POD method decomposes the fluctuating component of the velocity field into limited number of time-independent orthogonal modes $\varphi_n(x,y,z)$ and time-dependent orthonormal amplitude coefficients $\alpha_n(t)$, as expressed in equation (1)

$$u'(x,y,z,t_i)=\sum_{n=1}^{M}\alpha_n(t_i)\varphi_n(x,y,z) \tag{1}$$

POD has been widely applied as data reduction method for PIV experiments, yielding either a simplified representation of the structure of dominant fluctuations or supporting a reduced order reconstructed models based on a limited number of modes (Legrand et al. 2011, Van Oudheusden et al. 2005). The snapshot POD method, which was proposed by (Sirovich 1987), is applied to the current tomographic PIV experiment. The suitability of POD to the treatment of 3D data issued from tomographic PIV has been already shown in past works (Violato and Scarano 2013). Its first application to investigate the three-dimensional pattern resulting from the forced transition is given in the present study. The three velocity fluctuation components are arranged in the matrix below (equation (2)), in order to taking their correlation into account.

$$U=\begin{bmatrix} u_1^1 & u_1^2 & \cdots & \cdots & u_1^M \\ v_1^1 & v_1^2 & \cdots & \cdots & v_1^M \\ w_1^1 & w_1^2 & \cdots & \cdots & w_1^M \\ \vdots & \vdots & \vdots & \vdots & \vdots \\ \vdots & \vdots & \vdots & \vdots & \vdots \\ u_N^1 & u_N^2 & \cdots & \cdots & u_N^M \\ v_N^1 & v_N^2 & \cdots & \cdots & v_N^M \\ w_N^1 & w_N^2 & \cdots & \cdots & w_N^M \end{bmatrix} \tag{2}$$

Each POD mode is written as a linear combination of snapshots, as

$$\varphi_n(x,y,z)=\frac{1}{M\lambda_n}\sum_{i=1}^{M}\alpha_n(t_i)u'(x,y,z,t_i) \tag{3}$$

M is the number of snapshots. The corresponding eigenvalue of each modes λ_n represents its contribution to the total disturbance energy.

3. Time-averaged wake flow topology

The mean flow topology is examined with the iso-surfaces of non-dimensional streamwise vorticity ($\omega_x^* = \omega_x \times h / u_\infty$) at Re_h = 1170 and 465, as shown in Fig. 3. The major feature of a pair counter-rotating vortex pair can be observed emanating from the micro-ramp. From the side view, one can observe that this primary pair of vortices is lifted up when moving downstream by the self-induced velocity.

At Re_h = 1170 (Fig. 3(a)), as discussed by Ye et al. (2016a), after the rapid lift-up and decreased intensity, the primary vortex pair can no longer be distinguished from x/h = 40 (see Fig. 3(a) side view). The secondary vortex pair is formed beneath the primary pair, which is already present at the most upstream region of the measurement domain x/h = 4. At x/h = 25, a tertiary vortex pair is produced, together with further vortex pairs that appear on the outside when moving further downstream, expanding spanwise the streaky velocity distribution. The global time-averaged vortical structure resembles a wedge shape.

When decreasing Re_h to 465 (Fig. 3(b)), instead of undergoing a fast decay, the primary vortex pair appears to be initially lifted up and then continues downstream with no significant decay of its intensity. Starting from x/h = 10, each vortex of the primary pair bifurcates into two branches distributed vertically, which later re-connect into a single pair again and persist until the most downstream measurement location. A secondary pair of counter-rotating vortex appears from x/h = 14 at the spanwise side of the primary pair instead of beneath, and with opposite rotating direction. The formation of a tertiary vortex pair outwards of the secondary one is significantly delayed with respect to the case at higher Re_h as they appear from x/h = 45. The overall vortical structure, although similar to the previous case, has an inverted sign for the vorticity in the downstream region, which is due to the persistence of the primary vortex pair as opposed to them lifted away from the wall at Re_h = 1170. The formation of a wedge shape region is also delayed and only a tertiary pair is observed within the present measurement domain.

The spanwise modulation of momentum caused by the action of the streamwise vortices determines the spatial distribution of the low- and high-speed regions in the wake of the micro-ramp. The velocity deficit between the averaged streamwise velocity (u/u_∞) and the undisturbed boundary layer (u_{bl}/u_∞) is considered here as $u_d/u_\infty = (u - u_{bl})/u_\infty$ after the procedure introduced by Fisher and Choudhari (2004) at three y - z cross planes located at x/h = 5, 25, 52 (Fig. 4). The contour lines of streamwise velocity and selected projected streamlines are superimposed on the colour contours of the non-dimensional streamwise velocity deficit (u_d/u_∞).

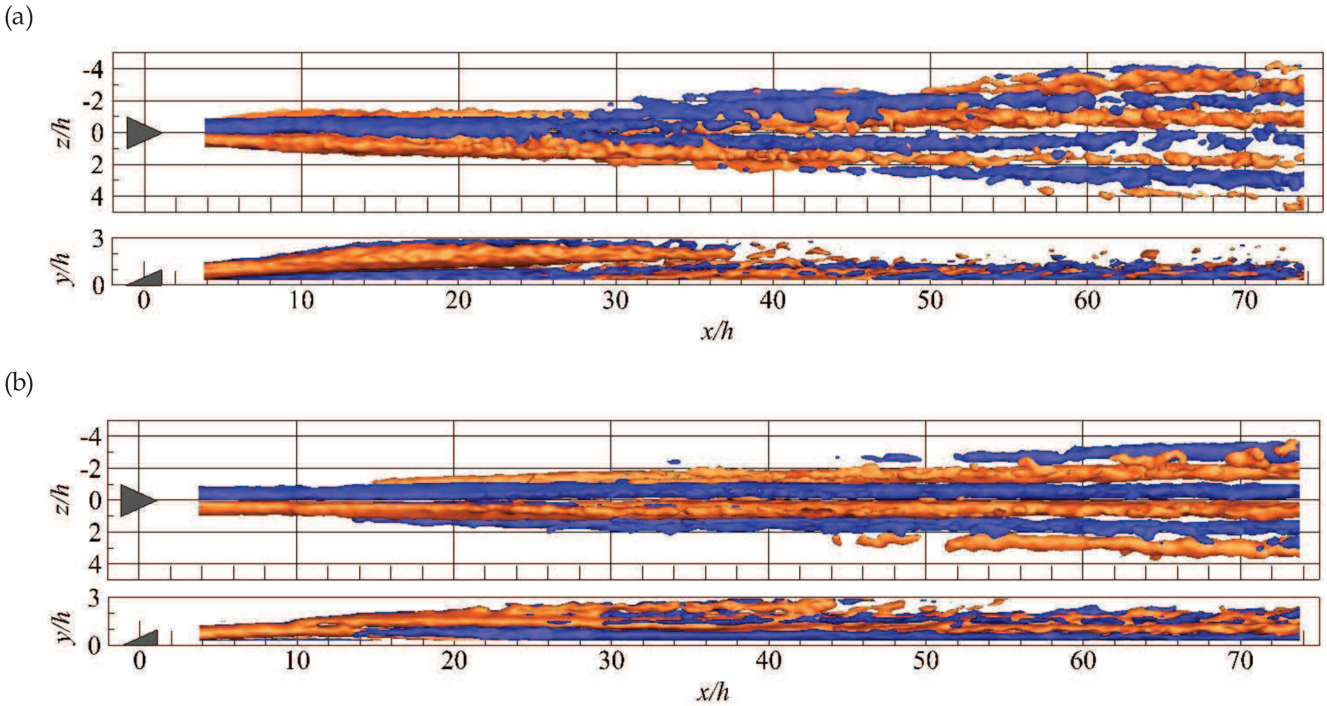

Fig. 3. Three-dimensional rendering of time-averaged streamwise vorticity (red and blue for clockwise and anticlockwise rotation vortices, $\omega_x{}^* = \pm 0.05$). (a) $Re_h = 1170$, (b) $Re_h = 465$. Top (top) and side (bottom) view.

Close to the micro-ramp (x/h = 5) for both Re_h, a pronounced low-speed region close to the symmetry plane bounding by two high-speed regions close to the wall is produced by the central upwash and lateral downwash motion of the primary vortices. Comparable magnitude of the low- and high-speed regions are produced, of $u_d = -0.53u_\infty$ and $0.24u_\infty$ at $Re_h = 1170$ and $u_d = -0.54u_\infty$ and $0.20u_\infty$ at $Re_h = 465$. A rapid decease in magnitude of the central low-speed region is observed at $Re_h = 1170$ (Fig. 4(a)), which lifts up and cannot be detected anymore at $x/h = 52$. A connection of the high-speed regions occurs at the most upstream region due to the fast lift-up process of the primary vortices and the early appearance of the secondary pair. The former regions merges at $x/h = 25$, leading to an increased magnitude of $0.51u_\infty$. Two newly formed sideward low-speed regions can be observed at this streamwise location, due to the sideward upwash motion produced by the secondary vortices. At $x/h = 52$, the flow demonstrates a relatively homogenous distribution of the high-speed region close to the wall. Nevertheless, two low-speed regions can still be detected on top of it with lower magnitude, indicating the persistence of sideward upwash motion. On the other hand, the central low-speed region persist till the most downstream measurement location for $Re_h = 465$, as well as the induced inflectional velocity profile, in favour of the amplification of turbulent fluctuations. The increase in magnitude of the high-speed regions (to $u_{dmax} = 0.33u_\infty$, at $x/h = 25$) is slower due to the late inception of secondary vortex pair and weaker downwash motion. The connection of high-speed region is postponed downstream to x/h = 52. Aside of the high-speed regions, two low-speed region with rather weak intensity can also be observed due to the upwash motion induced by the joint action secondary and tertiary vortex pair.

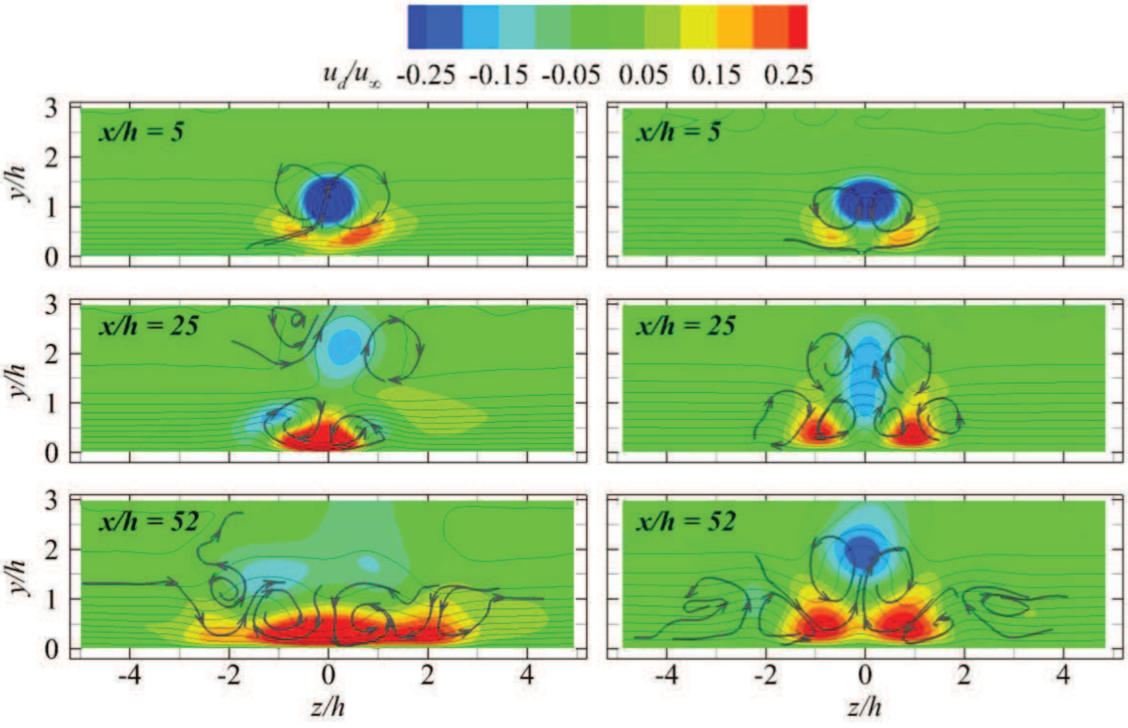

(a) $Re_h = 1170$ (b) $Re_h = 465$

Fig. 4. Streamwise velocity deficit u_d/u_∞ at $y - z$ cross planes, with contour lines of u/u_∞ = [0, 1] of 0.1 interval; flow topology shown with selected streamlines.

4. Evolution of velocity fluctuations

In order to quantitatively characterize the evolution of velocity fluctuations introduced by the micro-ramp, the integrated disturbance energy is tracked in the roughness wake, following the definition of Ergin and White (2006), as

$$e_{rms}(x) = \iint < u'(x, y, z) > /u_\infty d(y/h)d(z/h) \tag{4}$$

Special attention is paid to the difference of the disturbance energy produced by the change of Re_h. The streamwise evolution of e_{rms} at supercritical and critical Re_h is shown in Fig. 5. The evolution stages are separated with red and magenta lines for Re_h = 1170 and 465 respectively.

At Re_h = 1170, the amplitude of e_{rms} decreases rapidly from 0.025 to 0.012 from the most upstream region until x/h = 7 (stage I). Beyond x/h = 7, the integrated disturbance energy undergoes exponential growth when moving downstream. The growth rate of e_{rms} is calculated by performing linear fit to the semi-log profile, reaching the magnitude of 0.014 in the range of x/h = [7, 25] (stage II), following by a further intensification to 0.027 in x/h = [25, 46] (stage III). The streamwise location of the turning point of the growth rate coincides with the inception of tertiary vortex pair in the mean flow field. Further downstream ($x/h > 46$, stage IV), the growth of e_{rms} is retarded to a rate of 0.01, indicating that the flow becomes turbulent in this range. As proposed by Ye et al. (2016a), the transition mechanism is related to the velocity streak distribution produced by the secondary and tertiary vortex pair, leading to local inflectional instability. When evolving downstream, the amplitude of the velocity streaks decreases which is less susceptible to the growth of instability, leading to lower growth rate of fluctuations. A similar damping behavior of growth rate in the wake roughness element was also observed by Ergin and White (2006) and Bernardini et al. (2014). Ergin and White (2006) stated that the transition process is a competition between the growth of unsteady fluctuation and the relaxation of spanwise non-parallel flow towards Blasius condition. As the initial growth of the unsteady fluctuations is sufficiently large, although decays in the downstream region, the transition and breakdown to turbulence still occurs before the flow is restabilized.

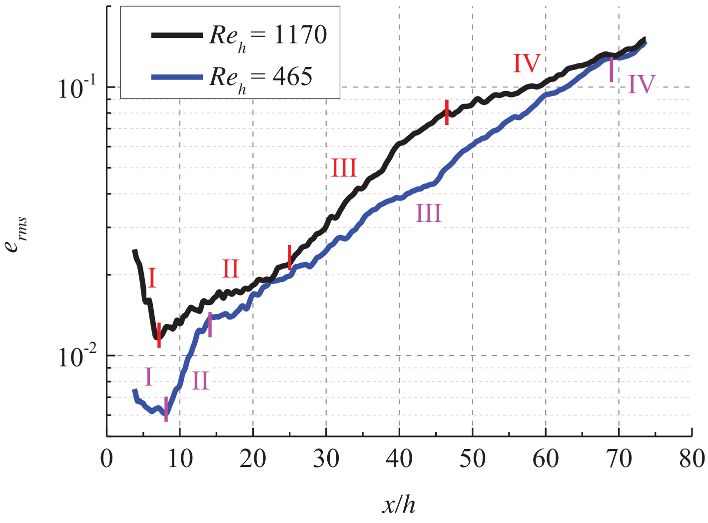

Fig. 5. Streamwise evolution of integrated disturbance energy.

Decreasing the Re_h to 465, the e_{rms} also amplifies, but showing lower magnitude in the entire streamwise range compared with Re_h = 1170, revealing that the micro-ramp wake is less unstable at lower Re_h. The behaviour of sharp decrease, following by a steep increase is also observed close to the micro-ramp, in the range of x/h = [3, 8] (stage I) and [8, 14] (stage II) respectively. The growth rate in the second stage (II) is significantly higher than that of higher Re_h. From x/h = 14, the integrated disturbance energy increases exponentially until x/h = 69 (stage III), with a lower growth rate of 0.018 with respect to supercritical condition. After this stage, the e_{rms} experience saturation as the flow approaches turbulent condition (stage IV). The disparity of e_{rms} between different Re_h vanishes. The late inception of the plateau stage (IV) remarks the onset of turbulence as well as transition is significantly delayed at low Re_h.

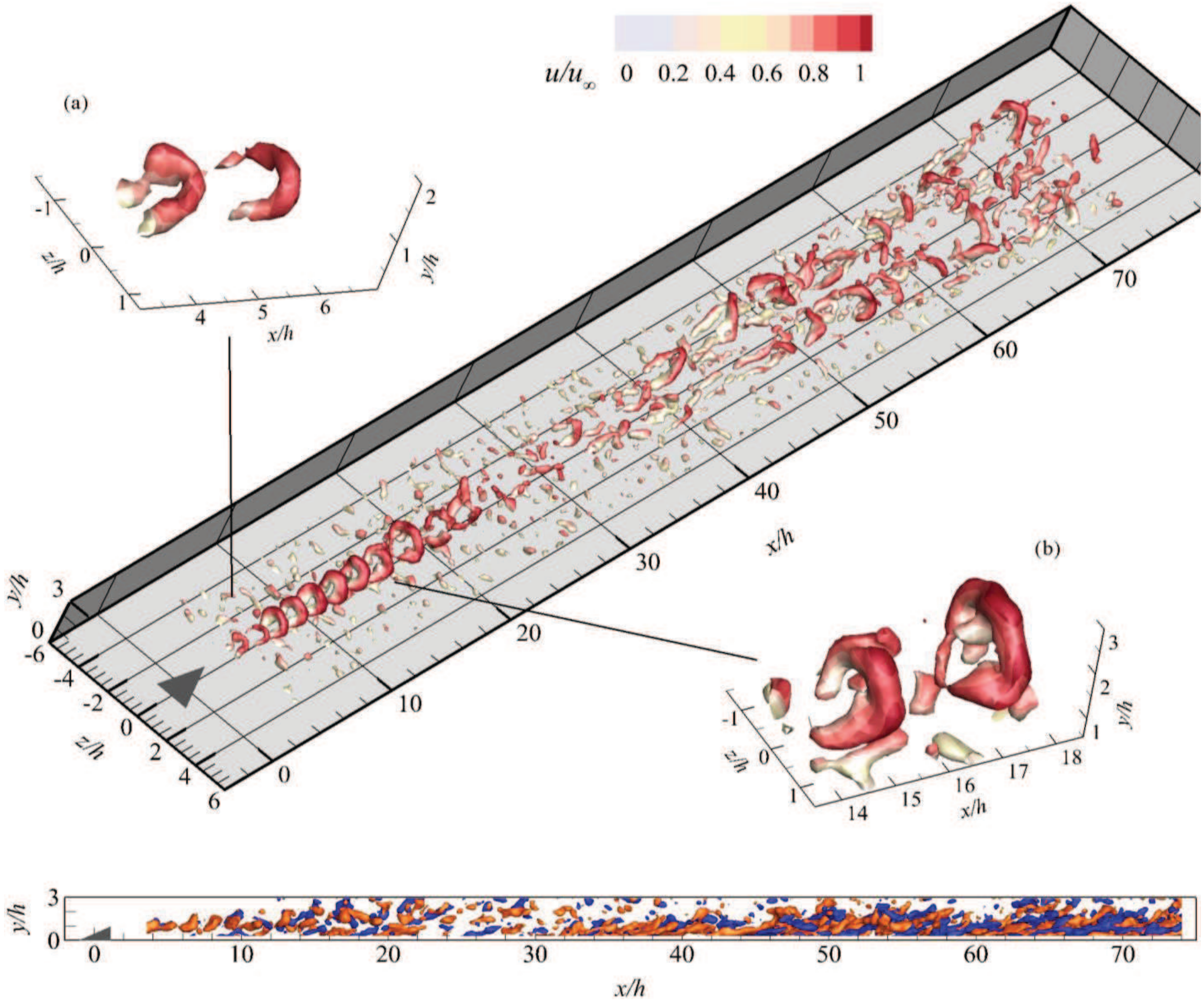

Fig. 6. The instantaneous flow pattern at Re_h = 1170, perspective view and (a)(b) detected by λ_2 criterion color-coded by u/u_∞; side view: streamwise vorticity, red and blue for clockwise and anticlockwise rotation vortices, ω_x^* = ±0.3.

4. Instantaneous flow topology

The interaction between micro-ramp and the laminar boundary layer produces a separated shear layer, where the velocity exhibits an inflectional profile susceptible to Kelvin-Helmholtz (K-H) instability. The latter instability leads to the formation of unstable waves in the form of hairpin-like vortices. The importance of K-H instability on transition process highly depends on

Reynolds number (Ergin and White 2006, Loiseau et al. 2014). In a recent study, Ye et al. (2016a) claimed that at supercritical Re_h, K-H vortices lose the spatial connection with the onset of turbulent wedge in the wake of micro-ramp, indicating K-H instability does not play a role in transition. In the current experiment, the pattern and evolution process of K-H vortices in the wake flow at different Re_h is visualized by the iso-surface of a vortex detection criterion by λ_2 (Jeong and Hussain 1995) and instantaneous streamwise vorticity (ω_x^*), as shown in Fig. 6 and Fig. 7.

At supercritical Re_h, the K-H vortices start to be active from $x/h = 5$ (Fig. 6), with initial wavelength of $\lambda/h = 1.45$. Besides sustained growth in size, the shape of K-H vortices changes from arch to hairpin (Fig. 6(a)), whose legs later connect at the bottom downstream, showing as a ring-shape (Fig. 6(b)) (Sun et al. 2014, Yan et al. 2014). The sudden increase in wavelength at $x/h = 18$ indicates the occurrence of vortex pairing. The vortices rapidly break down after the pairing region, losing coherence and periodicity downstream of $x/h = 25$. At $x/h = 35$, newly formed vortex structures show up in the near wall region with hairpin shape. The new hairpin vortices develop downstream with a spanwise spreading, resembling a wedge shape globally. The wedge shape vortex pattern is confirmed to be the turbulent wedge, indicating the onset of transition (Ye et al. 2016a).

At $Re_h = 465$, the shear layer at the interface of the wake and the free-stream exhibits a relatively steady state in the near wake of micro-ramp ($x/h = [0, 10]$) with only the primary streamwise vortex pair presenting. Downstream, a train of K-H vortices can be detected in a hairpin shape. The vortices are spaced at regular intervals with a longer initial wavelength of approximately $\lambda/h = 3.5$. The K-H vortices convect downstream while significantly growing in size and being stretched. The leg portion of the K-H is elongated and tends to move close to the wall, while the head portion lifts up and later detaches from the legs. A plateau part is formed in the leg, as shown in the side view in Fig. 7. Acarlar and Smith (1987) explained this plateau portion as the equilibrium of the interaction between two opposing effects, which are the shear effect that tends to rotate the hairpin towards the wall and the induced velocity of the two legs. In between of two neighbouring hairpins legs, a buffer vortex structure is formed with opposite rotation direction due to the mutual induction effect of the legs, as shown by the iso-surface of streamwise vorticity ω_x^* in Fig. 7(b). The leg-buffer vortices draw vorticity from the bifurcated shear layer and grow in size. They move away from the symmetry plane and tend to connect between sequential vortices, corresponding to the secondary vortex structure in the mean flow organisation. The further increase in intensity of the leg-buffer vortices gives rise to another unique large leg-shape vortex structure outwards. The strong sideward ejection event transports low momentum flow to the outer boundary layer, which is susceptible to the growth of perturbation. The combined vortex packet starts from x/h = 52 in Fig. 7(b) resemble the feature of U-shape vortex, indicating the delayed onset of transition (Singer and Joslin 1994). The turbulent wedge is not detected. Unlike the paring and rapid distortion process at Re_h = 1170, the K-H vortices here appear to persist over a significantly longer streamwise distance. They also seem to participate in the formation of U-shape vortex packet associate to the onset of transition. The latter indicates that close to the critical regime of Re_h, K-H instability plays a role in the route to forced transition for the micro-ramp geometry.

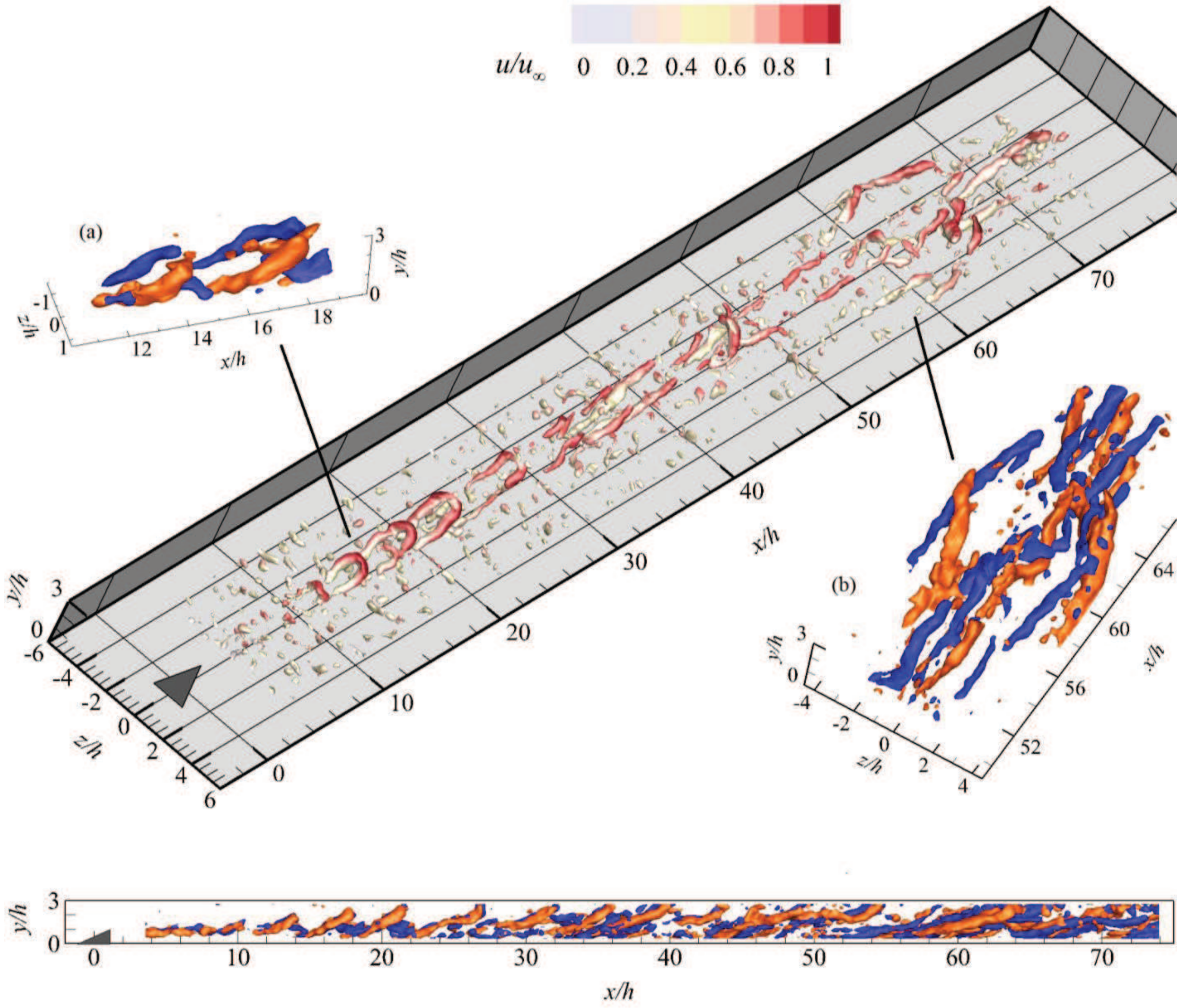

Fig. 7. The instantaneous flow pattern at Re_h = 465, perspective view detected by λ_2 criterion color coded by u/u_∞; side view and (a)(b): streamwise vorticity, red and blue for clockwise and anticlockwise rotation vortices, ω_x^* = ±0.3.

In summary, at Re_h = 465, the primary vortices of time-averaged flow as well as the K-H rollers in the instantaneous flow persist over a longer streamwise range. However, the onset of secondary and tertiary vortex pair is postponed downstream. The transition process is significantly delayed as the turbulent wedge does not appear in the current measurement domain. The onset location and relevant properties of the aforementioned vortical structures at both Re_h are summarized in Tab. 1.

Tab. 1. Comparison between vortical structures at different Re_h.

Re_h.	1170	465
Streamwise range of primary vortices	< 40	< 75
Onset of the secondary vortices	< 4	14
Onset of the tertiary vortices	25	45
Wavelength of K-H vortices	1.45	3.5
Streamwise range of K-H vortices	[5, 25]	[10, 75]

5. POD analysis

In the present study, the snapshot POD method is applied to three-dimensional velocity field to reveal the most energetic flow structures as well as their contribution to the growth of total disturbance energy, which possibly lead to the onset of transition. The analysis is performed in a subdomain before the start of fully turbulent flow at both supercritical and critical Re_h, as the later contains high turbulent kinetic energy, which would mask the features in the laminar and transitional state. Consequently, the domain is reduced to x/h < 45 and 60 for Re_h = 1170 and 465 respectively. The contribution of 45 modes to the total disturbance energy is demonstrated in Fig. 8. Different from the POD analysis of the wake flow of the blunt body (Van Oudheusden et al. 2005) or jet flows (Kirby et al. 1990), in which the large amount of energy is captured by a small number of eigenmodes (usually first two modes), small energy variation between low- and high order modes is observed in the current analysis. The distinction can attribute to the fact that the observed flow structures in the transitional boundary layer forced by surface roughness are highly multiscale and non-linear, allocating energy to high-order modes. Moreover, the relative disturbance energy of each single mode does not directly represent its importance in the transition process. On the other hand, the correspondence between the topology of POD modes and the development of specific flow instability becomes critical in identifying the contribution of the modes to transition. As at Re_h = 1170 the large-scale Kelvin-Helmholtz type vortices becomes less predominant, and survives in shorter streamwise range, the energy distribution is further flattened with 24% of the total energy captured by the first 20 eigenmodes, lower than 36% at $Re_h = 465$.

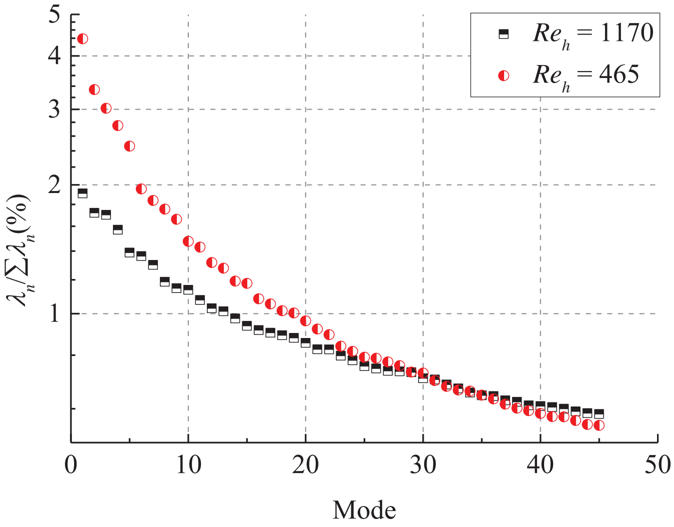

Fig. 8. Relative energy distribution of first 45 POD modes.

4.1 Supercritical condition: $Re_h = 1170$

The first three POD modes are selected to depict the flow features, as they contained highest amount of energy, being considered as good representation of the dominant unsteady behaviour of the flow. The rest modes show similar distribution of velocity fluctuations, corresponding to the same features, thus not being discussed in detail. The iso-surface of normalized streamwise velocity fluctuation component is shown in Fig. 9.

In the near wake of micro-ramp ($x/h < 20$), the flow is dominated by the K-H vortices in the instantaneous flow. It is expected that the former structure contributes to high level of velocity fluctuations within this streamwise range. In mode 1 and 2, the distribution of velocity fluctuations is topologically similar. The back-facing separate produced by the mciro-ramp leads to velocity fluctuation patches at $x/h < 5$. Soon after that (x/h = [5 18]), the shape of the iso-surface of high velocity fluctuations shows in the form of distinct patches of alternating sign. A quarter wavelength spatial shift of the two modes can be identified with the vector map at the symmetry plane, as shown in Fig. 10. The spatial correlation between the two modes reveals the presence of convective K-H rollers in the wake (Lengani et al. 2014). The starting of the shedding phenomenon is detected by the first velocity fluctuation maxima at $x/h = 5$, with an initial wavelength of $\lambda_{s0}/h = 1.45$, reaching good agreement with the wavelength of K-H vortices from instantaneous flow topology. Furthermore, the patches exhibit good spanwise symmetry with respect to the symmetry plane. The scenario is similar to the varicose mode obtained from stability analysis (Loiseau et al. 2014), contributing to the formation of hairpin vortices. Although initially appears at the wake centre, the varicose mode propagates and occupies the whole span before fades away. However, the velocity fluctuation patches in POD mode 1 and 2 is confined within a limited spanwise range. The intensity of the patches start to attenuate from *x/h* = 18, becoming negligible beyond *x/h* = 22. Moving downstream to *x/h* = 28 in mode 1, new patches appear close to the wall, shifting away from the symmetry plane, with alternative positive and negative sign as well. The patches are oblique to the streamwise direction, initiating the amplification of turbulent fluctuations. In mode 2, the new patches are paralleled to the streamwise direction in the beginning (*x/h* = (22, 28)), turning into the oblique pattern from *x/h* = 28. The oblique patches spread in the spanwise direction and resemble a wedge shape globally, contaminating the laminar flow. The former patches are regarded as the precursor of the turbulent wedge in the downstream region. In addition, the coexistence of the patches corresponding to the K-H vortices and the near-wall patches in the same mode indicates their correlation.

(a) Mode 1

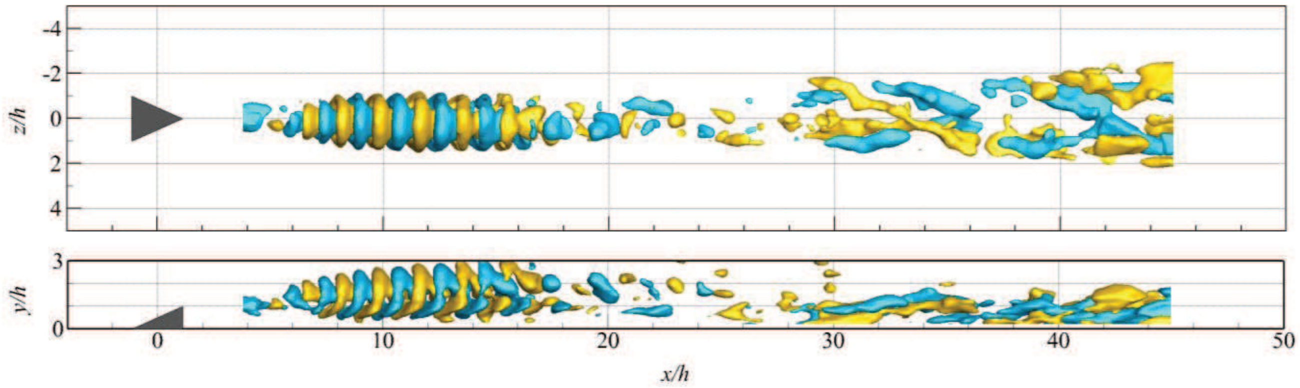

(b) Mode 2

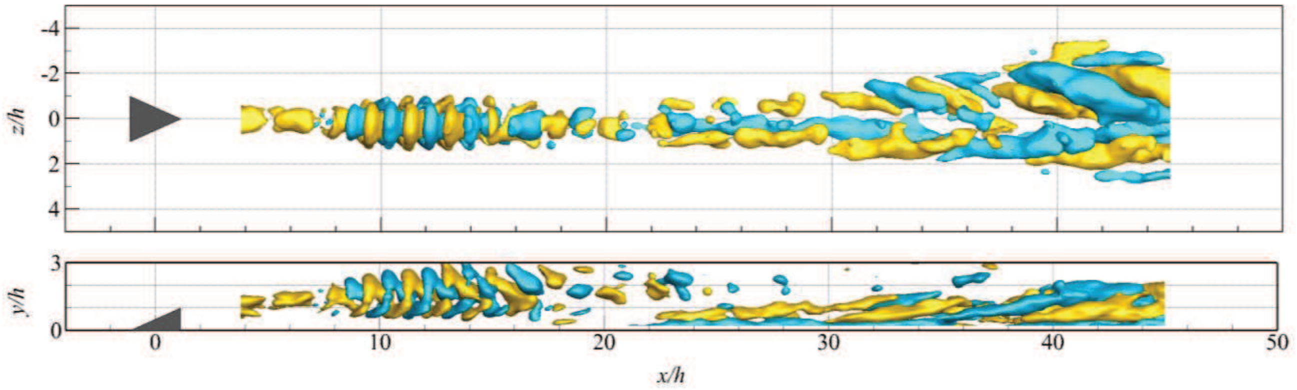

(c) Mode 3

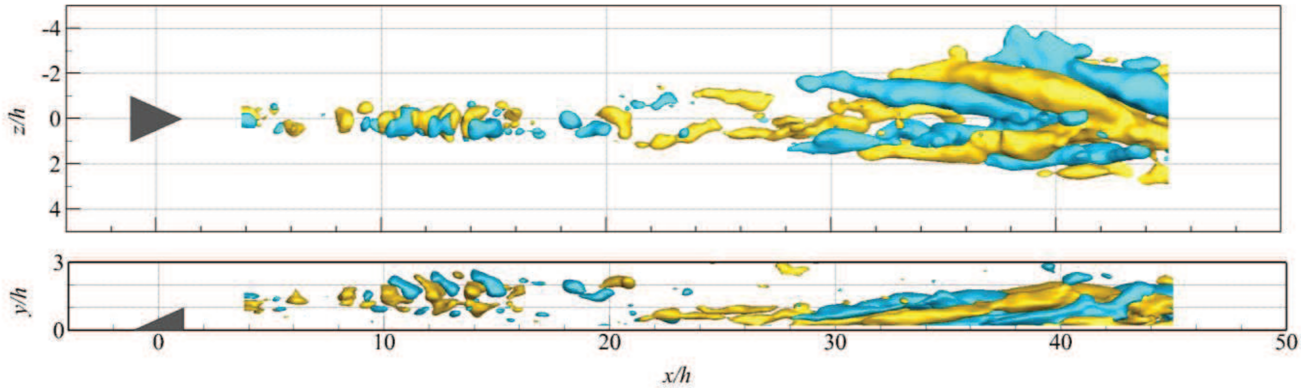

Fig. 9. Streamwise velocity component of POD modes at $Re_h = 1170$ ($u'/u_\infty = 1.2\times10^{-4}$).

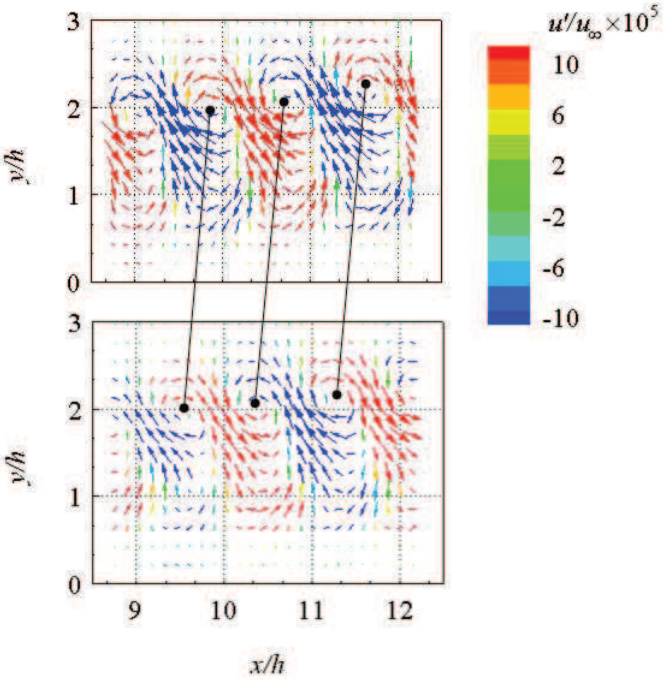

Fig. 10. *x*-*y* cross-sectional vector maps of mode 1 and 2 at $z/h = 0$,

color-coded by the streamwise velocity component (u'/u_∞)

Different velocity fluctuation structures are presented in mode 3 in the near wake, as the patches of alternating sign tend to distribute in a staggered pattern, losing the spanwise symmetry (Fig. 9(c)). The inception of the velocity fluctuation patches postpones to $x/h = 8$, with a larger initial wavelength λ_{a0}/h of 1.7 due to higher convective velocity at the former location. No pair of eigenmode arises in this case, indicating its stationary nature. The magnitude of velocity fluctuations is significant lower comparing with symmetric modes (1 and 2). Similar to what observed in the sinuous instability mode (Loiseau et al. 2014), the asymmetric mode is assumed to modulate the flow field into sinuous wiggling pattern. Consequently, the shape of hairpin vortices caused by the asymmetric mode loses the varicose symmetry, demonstrating a pulsating motion. Starting from $x/h = 21$, the oblique patches close to the wall can also be detected, resembling the spatial distribution as that in mode 1 and 2. Similarly, the asymmetric patches are correlated to the oblique patches as well.

The above analysis suggests that the vortical dynamics close to the micro-ramp should be a combination of shedding and wiggling motion, as both symmetric and asymmetric mode arises. However, as the magnitude of the asymmetric mode is comparably lower than the symmetric mode, the sinuous modulation to the K-H vortices is not obvious in the instantaneous flow.

A quantitative assessment of the correlation between the upstream symmetric/asymmetric and downstream oblique patches are performed by comparing the evolution of integrated disturbance energy e_{rms} produced by mode 1 and 2 in combination (symmetric), and mode 3 (asymmetric), as shown in Fig. 11. The streamwise velocity fluctuations are reconstructed using equation (1). The R.M.S of the velocity fluctuations is computed over 200 instantaneous snapshots. In the near wake ($x/h < 20$), the symmetric modes dominate the disturbance energy, while the contribution of asymmetric mode is one order lower. For the symmetric modes, the disturbance grows quickly after the birth of K-H vortices at $x/h = 5$, reaching the maximum amplitude at $x/h = 11$, following by a rapid decrease extending up to $x/h = 18$. The disturbance energy stays relatively constant moving downstream. Starting from $x/h = 25$, the e_{rms} of asymmetric mode undergoes steep increase due to the formation of oblique patches, rising up beyond the level of symmetric modes at $x/h = 33$. Whereas the second ascending of the later modes occurs downstream at $x/h = 36$, reaching lower maximum magnitude comparing with asymmetric mode.

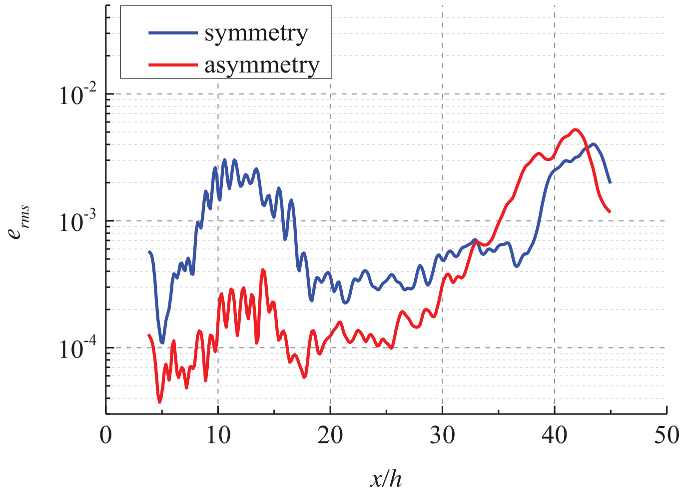

Fig. 11. Streamwise evolution of e_{rms} of symmetric (1 and 2) and asymmetric (3) modes at $Re_h = 1170$.

Further reconstruction of the velocity fluctuations has been made up to 15 POD modes, taking into account 20% of the total disturbance energy. Particularly, the velocity fluctuations induced by the modes showing symmetric and asymmetric spatial distribution are picked out and summed up separately. The streamwise evolution of integrated disturbance energy is compared in Fig. 12. The energy disparity between the symmetric and asymmetric modes decreases in the near wake (x/h < 18). The energy of both modes saturates, reaching a plateau of the same disturbance energy magnitude in x/h = [18 30]. Beyond x/h = 30, the growth rate of the asymmetric modes increases with respect to mode 3, while that of symmetric mode remains the same as mode 1 and 2, leading to a larger energy difference in the downstream region. As a result, although the asymmetric patches containing lower disturbance energy in the upstream region, its related oblique patches captures larger amount of energy comparing to that of symmetric patches, indicating its larger contribution to the inception of turbulent wedge as well as transition.

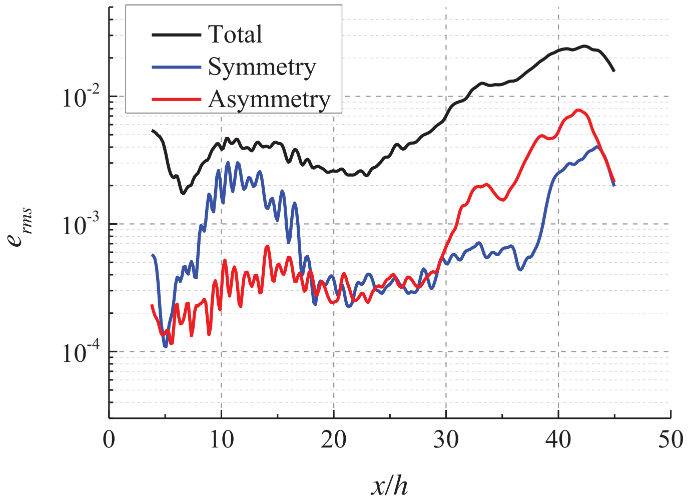

Fig. 12. Streamwise evolution of e_{rms} of 15 modes at Re_h = 1170.

4.2 Critical condition: Re_h = 465

At critical Re_h, the patches of the most energetic POD mode convert into an asymmetric spatial distribution as shown in Fig. 13(a). Compared with mode 3 at supercritical condition, a more pronounced spanwise shift of velocity fluctuation patches of alternating sign can be observed around the symmetry plane, indicating a stronger sinuous modulation to the central low-speed region by this mode. The asymmetric mode starts from the most upstream of the measurement domain, while the inception of the staggered distributed patches moves downstream to x/h = 10. The initial wavelength of the patches of the same sign is λ_{a0}/h = 3, lower than that of the K-H vortices in the instantaneous flow. Instead of limiting close to the symmetry plane, the asymmetric mode spreads in the spanwise direction by inducing positive and negative velocity fluctuation streaks at the side, contributing to the unsteadiness of the spanwise shear layer between neighbouring low- and high-speed regions in the mean flow (see **Fig. 4**). The velocity fluctuation streaks persist till the downstream end of the domain, maintaining high amplitude. The structures resemble a wedge shape globally. The oblique patches do not emerge in this mode.

Similar to the observation at supercritical condition, pairing of mode 2 and 3 occurs in phase quadrature (see Fig. 13(b)(c) and Fig. 14), yielding the occurrence of shedding phenomenon of the K-H vortices. Longer streamwise distance from the micro-ramp is required for the onset of mode 2 and 3. The initial wavelength λ_{s0}/h of the former modes is 3.5, which is identical to that of K-H vortices in the instantaneous flow. The patches are stretched and extend towards the wall. The spanwise propagation of the patches is initiated by the generation of velocity fluctuation filaments close to the wall. The patches correspond to vortex shedding survive for longer streamwise distance comparing with supercritical condition, downstream to x/h = 45 and 50 for mode 2 and 3 respectively. From this location on, oblique patches of larger size in spatial extent can be detected, showing good spanwise symmetry. Although the inception is delayed, the topology of the new patches coincides with that at supercritical Re_h.

(a) Mode 1

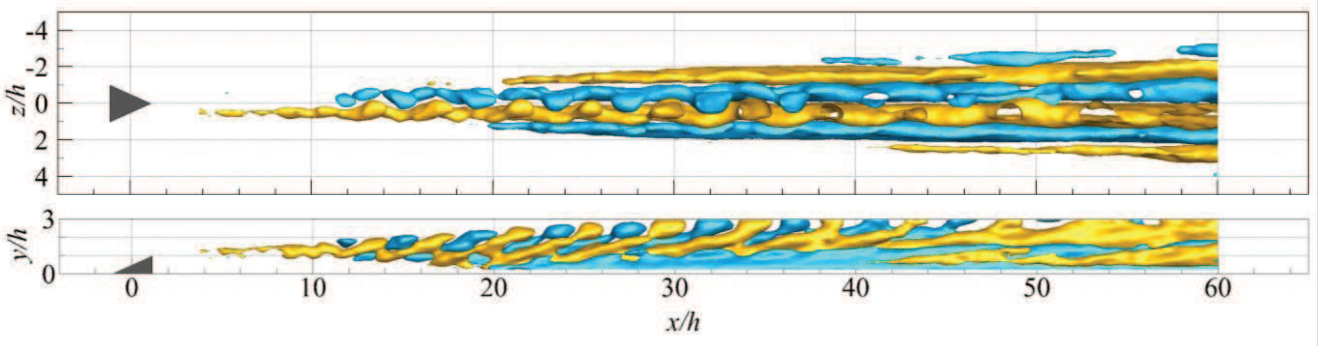

(b) Mode 2

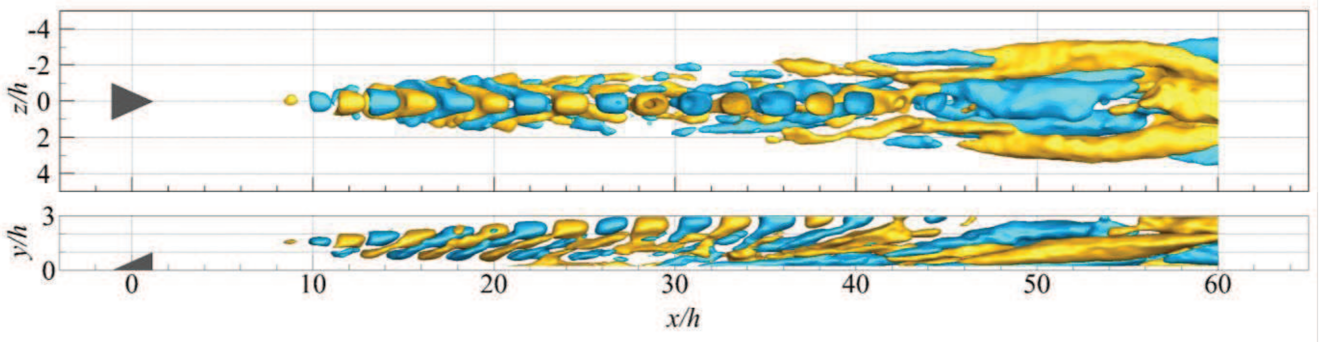

(c) Mode 3

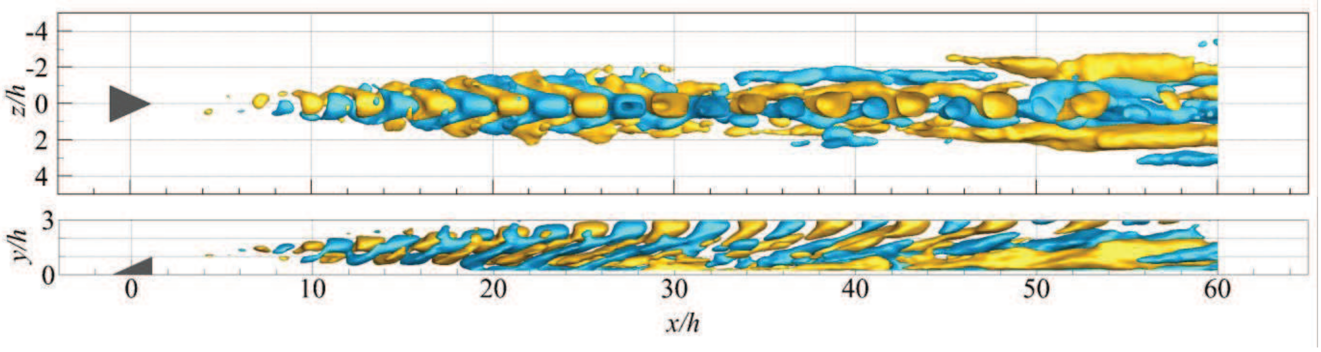

Fig. 13. Streamwise velocity component of POD modes at $Re_h = 465$ ($u'/u_\infty = 1.0\times10^{-4}$).

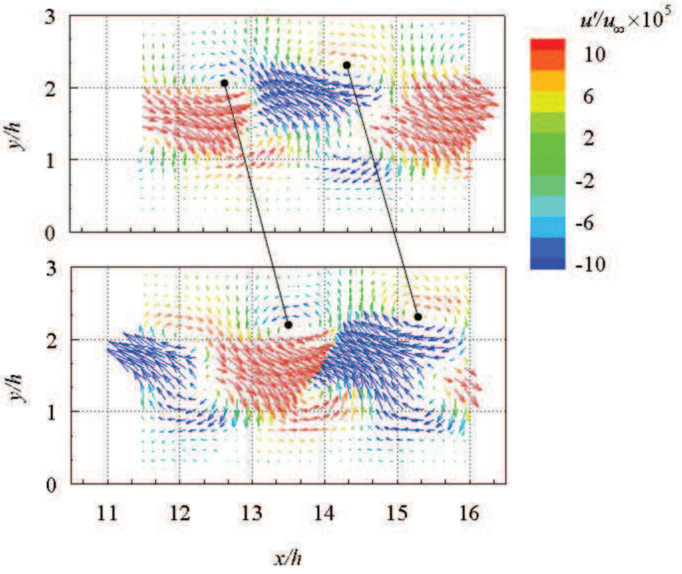

Fig. 14. x-y cross-sectional vector maps of mode 2 and 3 at $z/h = 0$,

color-coded by the streamwise velocity component (u'/u_∞).

The streamwise evolution of the integrated disturbance energy at critical $Re_h = 465$ is shown in Fig. 15. For the asymmetric mode, e_{rms} undergoes exponential growth starting from the upmost region of the measurement domain and saturates from $x/h = 40$. Although the symmetry modes captures larger portion of the disturbance energy in the upstream region ($x/h < 30$), higher magnitude of e_{rms} is observed for asymmetric mode in the range of $x/h = [30, 46]$ due to its rapid intensification. The inception of the oblique patches in the symmetry mode lead to the second increase of turbulent fluctuation energy at $x/h = 45$, reaching saturation of the similar magnitude as the asymmetry mode at $x/h = 50$.

By taking the first 7 POD modes into account, which also contain 20% of total disturbance energy, it is found that only the first mode shows asymmetric distribution, whereas more mode pairs of symmetry type emerge. The overall integrated disturbance energy of all the symmetric modes is higher than that of the asymmetry mode in the whole investigated domain. As the oblique patches in the symmetric mode introduce higher amplitude of velocity fluctuations in *x/h* = [45, 60], its amplification possibly lead to transition.

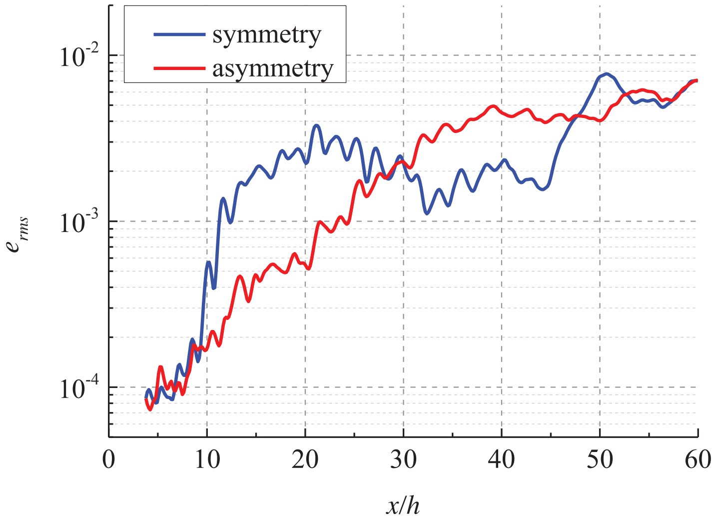

Fig. 15. Streamwise evolution of e_{rms} of symmetric (2 and 3) and asymmetric (1) mode at Re_h = 465.

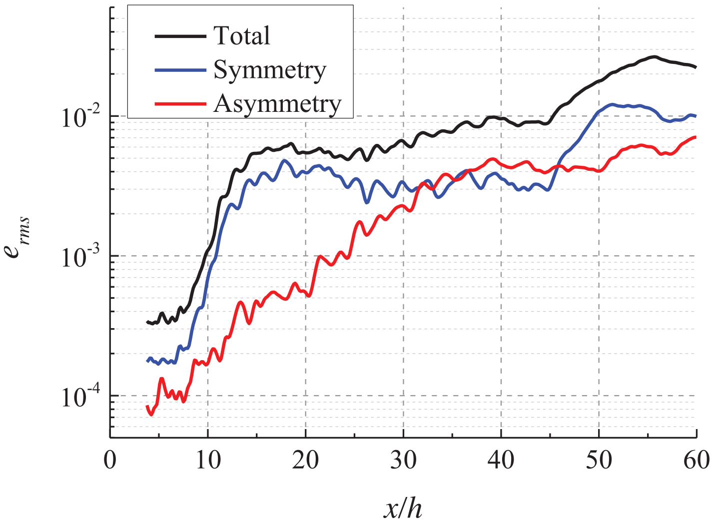

Fig. 16. Streamwise evolution of e_{rms} of 7 modes at Re_h = 465.

Conclusions

Tomographic PIV measurements on micro-ramp induced boundary layer transition in incompressible flow are performed at both critical and supercritical Re_h. Strong dependence of vortical dynamics in the micro-ramp wake on Reynolds number has been found, which influence the evolution process towards transition.

The time-averaged wake flow topology features multiple pairs of streamwise vortex pairs at both Re_h. At supercritical Re_h of 1170, as reported by Ye et al. (2016a), the sideward low-speed regions induced by the upwash motion due to secondary and tertiary vortex pairs is susceptible to local inflectional instabilities, leading to the production of turbulent fluctuations and the onset of transition. At critical condition (Re_h = 465), the primary vortices persist till the most downstream region of the measurement domain, inducing central low-speed region of high amplitude of velocity deficit. The central inflectional velocity profile leads to the growth of velocity fluctuations due to Kelvin-Helmholtz instability. The transition process is significantly delayed at low Re_h.

Proper Orthogonal Decomposition is proved to be a feasible data reduction technique to highlight the dominant flow features in the three-dimensional transitional boundary layer. Two dominant types of modes are obtained from the POD analysis. The symmetric mode pair corresponds to the shedding phenomenon of K-H vortices, while the asymmetric mode leads to a sinuous wiggling around the wake centreline. In the downstream region, oblique patches of velocity fluctuations can be detected, giving rise to the amplification of turbulent fluctuation energy, which leads to the onset of transition. The correlation of the former POD modes with the transition process strongly depends on Re_h. At supercritical Re_h, the asymmetric mode contributes higher amplitude of disturbance energy to the oblique patches, playing the dominant role on transition. Whereas at critical Re_h, the symmetric mode takes over the position, denoting greater contribution.

Reference

- Acarlar MS, Smith CR (1987) A study of hairpin vortices in a laminar boundary layer. Part 1. Hairpin vortices generated by a hemisphere protuberance. J Fluid Mech 175:1-41
- Andersson P, Brandt L, Bottaro A, Henningson DS (2001) On the breakdown of boundary layer streaks. J Fluid Mech 428:29-60
- Atkinson C, Soria J (2009) An efficient simultaneous reconstruction technique for tomographic particle image velocimetry. Exp Fluids 47:553-568
- Bernardini M, Pirozzoli S, Orlandi P, Lele SK (2014) Parameterization of boundary-layer transition induced by isolated roughness elements. AIAA J 52:2261-2269

- Ergin FG, White EB (2006) Unsteady and transitional flows behind roughness elements. AIAA J 44:2504-2514
- Fransson JHM, Brandt L, Talamelli A, Cossu C (2004) Experimental and theoretical investigation of the nonmodal growth of steady streaks in a flat plate boundary layer. Phys Fluids 16:3627-3638
- Jeong J, Hussain F (1995) On the identification of a vortex. J Fluid Mech 285:69-94
- Kirby M, Boris J, Sirovich L (1990) An eigenfunction analysis of axisymmetric jet flow. J Comput Phys 90:98-122
- Klebanoff PS, Cleveland WG, Tidstrom KD (1992) On the evolution of a turbulent boundary layer induced by a three-dimensional roughness element. J Fluid Mech 237:101-187
- Klebanoff PS, Schubauerand GB, Tidstrom KD (1955) Measurements of the effect of two-dimensional and three-dimensional roughness elements on boundary-layer transition. Journal of the Aeronautical Sciences 22:803-804
- Klebanoff PS, Tidstrom KD (1972) Mechanism by which a two-dimensional roughness element induces boundary-layer transition. Phys Fluids 15:1173-1188
- Landahl MT (1990) On sublayer streaks. J Fluid Mech 212:593-614
- Legrand M, Nogueira J, Tachibana S, Lecuona A, Nauri S (2011) Flow temporal reconstruction from non time-resolved data part ii: Practical implementation, methodology validation, and applications. Exp Fluids 51:861-870
- Lengani D, Simoni D, Ubaldi M, Zunino P (2014) Pod analysis of the unsteady behavior of a laminar separation bubble. Exp Therm Fluid Sci 58:70-79
- Loiseau J-C, Robinet J-C, Cherubini S, Leriche E (2014) Investigation of the roughness-induced transition: Global stability analyses and direct numerical simulations. J Fluid Mech 760:175-211
- Lumley JL (1967) The structure of inhomogeneous turbulence. In: Yaglom AM and Tatarski VI (eds) Atmospheric turbulence and wave propagation. Nauka, Moscow, pp. 166-178
- Lynch KP (2015) Advances in time-resolved tomographic particle image velocimetry. Doctor of Philosophy Delft University of Technology, The Netherlands
- Singer BA, Joslin RD (1994) Metamorphosis of a hairpin vortex into a young turbulent spot. Phys Fluids 6:3724-3736
- Sirovich L (1987) Turbulence and the dynamics of coherent structures part ii: Symmetries and transformations. Quarterly of Applied mathematics 45:573-582
- Sun Z, Scartino F, Van Oudheusden BW, Schrijer FFJ, Yan Y, Liu C (2014) Numerical and experimental investigations of the supersonic microramp wake. AIAA J 52:1518-1527
- Tani I (1969) Boundary-layer transition. Annual Review of Fluid Mechanics 1:169-196

- Tani I, Komoda H, Komatsu Y, Iuchi M (1962) Boundary-layer transition by isolated roughness. Rep. 375, Aeronautical Research Institute UoT
- van Driest ER, McCauley WD (1960) The effect of controlled three-dimensional roughness on boundary-layer transition at supersonic speeds. Journal of the Aerospace Sciences 27:261-271
- Van Oudheusden BW, Scarano F, Van Hinsberg NP, Watt DW (2005) Phase-resolved characterization of vortex shedding in the near wake of a square-section cylinder at incidence. Exp Fluids 39:86-98
- Violato D, Scarano F (2013) Three-dimensional vortex analysis and aeroacoustic source characterization of jet core breakdown. Phys Fluids 25:015112
- Von Doenhoff AE, Braslow AL (1961) The effect of distributed surface roughness on laminar flow. In: Lachmann GV (ed) Boundary Layer and Flow Control. Pergamon, pp. 657-681
- Westerweel J, Scarano F (2005) Universal outlier detection for piv data. Exp Fluids 39:1096-1100
- Wieneke B (2008) Volume self-calibration for 3d particle image velocimetry. Exp Fluids 45:549-556
- Yan Y, Chen C, Wang X, Liu C (2014) Les and analyses on the vortex structure behind supersonic mvg with turbulent inflow. Appl Math Model 38:196-211
- Ye Q, Schrijer FFJ, Scarano F (2016a) Boundary layer transition mechanisms behind a micro-ramp. J Fluid Mech 793:132-161
- Ye Q, Schrijer FFJ, Scarano F (2016b) Geometry effect of isolated roughness on boundary layer transition investigated by tomographic piv. Int J Heat Fluid Flow, accepted